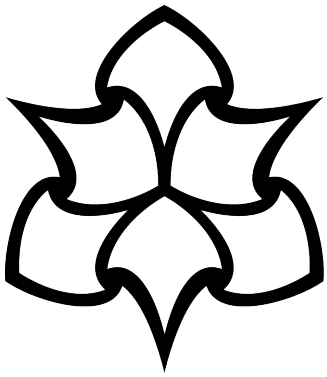

Results in Physics 12 (2019) 1238–1244

Contents lists available at ScienceDirect

Results in Physics

journal homepage: www.elsevier.com/locate/rinp

Synthesis of boron doped $C_3N_4/NiFe_2O_4$ nanocomposite: An enhanced visible light photocatalyst for the degradation of methylene blue

Surabhi Kamal[a], Sridharan Balu[a], Selvakumar Palanisamy[a,b,*], Kasimayan Uma[c], Vijayalakshmi Velusamy[b], Thomas C.K. Yang[a,c,*]

[a] Department of Chemical Engineering and Biotechnology, National Taipei University of Technology, Taipei 106, Taiwan
[b] Division of Electrical and Electronic Engineering, School of Engineering, Manchester Metropolitan University, Chester Street, Manchester M1 5GD, United Kingdom
[c] Precision Analysis and Materials Research Centre, National Taipei University of Technology, Taipei 106, Taiwan

ARTICLE INFO

Keywords:
Thermal condensation
Sol-gel method
$BCN/NiFe_2O_4$ nanocomposite
Visible-light photocatalyst
Methylene blue

ABSTRACT

In this paper, we report the synthesis of boron doped $C_3N_4/NiFe_2O_4$ nanocomposite and its application as a visible-light photocatalyst for the degradation of methylene blue (MB). Boron-doped C_3N_4 (BCN) was prepared by simple thermal condensation of dicyandiamide with boric acid, and $NiFe_2O_4$ nanoparticles were prepared by the simple sol-gel method. The as-synthesized nanocomposite materials were characterized and confirmed by the X-ray diffraction spectroscopy, Fourier-transform infrared spectroscopy, field-emission scanning electron microscopy, transmission electron microscopy, UV–Visible diffuse reflectance spectroscopy, X-ray photoelectron spectroscopy, and photoluminescence spectroscopy. The photocatalytic activity of $BCN/NiFe_2O_4$ nanocomposite was evaluated towards the degradation of MB in the presence of visible light irradiation. The obtained results confirmed that $BCN/NiFe_2O_4$ composite has higher degradation efficiency (98%) than that of BCN and $NiFe_2O_4$.

Introduction

The major environmental issues are directly caused by the growth of industrialization with increasing world population leading to depletion of air, soil and water systems [1]. The untreated waste and pollutants discharged from these industries have a high concentration of organic contaminants, salts, dyes, and heavy metals [2]. Among all, dyes and pigments are considered as toxic pollutants due to their harmful effect on to the hydrosphere, agriculture and living organisms [3]. Furthermore, the dye-containing effluents are more stable and non-biodegradable due to its complex structure [4]. To date, different methods have been employed to remove the dyes such as photocatalysis [5,6], catalytic treatment [7] and chemical treatment [8]. Over the past few decades, the semiconductor photocatalytic technology has emerged as an alternate procedure for the elimination of organic pollutants and to make the pollutant mineralize into CO_2 and H_2O [9].

Carbon nitride ($g\text{-}C_3N_4$) is a well-known semiconductor material, has attracted much attention in a wide range of fields due to its high chemical stability [10], low cost [11], less toxicity [12] and significant bandgap (2.7–2.8 eV) [10]. More recently, $g\text{-}C_3N_4$ incorporated metals [13,14], metal oxides [13,15] and non-metals [13,16] have shown enhanced photocatalytic performance towards the degradation organic dyes than pristine $g\text{-}C_3N_4$. Also, the introduction of non-metals such as boron or sulfur has maintained the metal-free nature of $g\text{-}C_3N_4$ because of their high ionization energy and high electronegativity [17]. Among different non-metals, boron is a lightweight element and forms a stable chemical bond with the $g\text{-}C_3N_4$ [18]. Due to the discussed unique properties, it can often alter the photocatalytic activity of $g\text{-}C_3N_4$ when combined with other semiconductor materials [19]. The useful addition of semiconductor materials into the boron doped $g\text{-}C_3N_4$ (BCN) matrix can reduce the energy band gap and electronic structure which may eventually increase the electron-hole separation and the catalytic activity [20]. More recently, the spinel ferrite structures (MFe_2O_4, M = Zn, Ni, Co) have found significant interest in the application of organic dye degradation [5,21] and water splitting reactions [22,23]. In particular, nickel ferrite ($NiFe_2O_4$) is a well-known visible-light semiconductor and having a narrow band gap of 2.19 eV with decent photocatalytic stability [24]. Recent studies revealed that the photocatalytic activity of $g\text{-}C_3N_4$ had been improved in the visible light region when combined with noble metal and metal oxides [25]. The heterojunction structure of the semiconductor composites is the main reason for the enhanced photocatalytic activity. However, $NiFe_2O_4$ decorated BCN nanocomposite has never been used for the photocatalytic applications. Given the above points, the integration of unique

* Corresponding authors at: Department of Chemical Engineering and Biotechnology, National Taipei University of Technology, Taipei 106, Taiwan.
E-mail addresses: prmselva@gmail.com, prmselva@mail.ntut.edu.tw (S. Palanisamy), ckyang@mail.ntut.edu.tw (T.C.K. Yang).

https://doi.org/10.1016/j.rinp.2019.01.004
Received 21 November 2018; Received in revised form 27 December 2018; Accepted 2 January 2019
Available online 06 January 2019

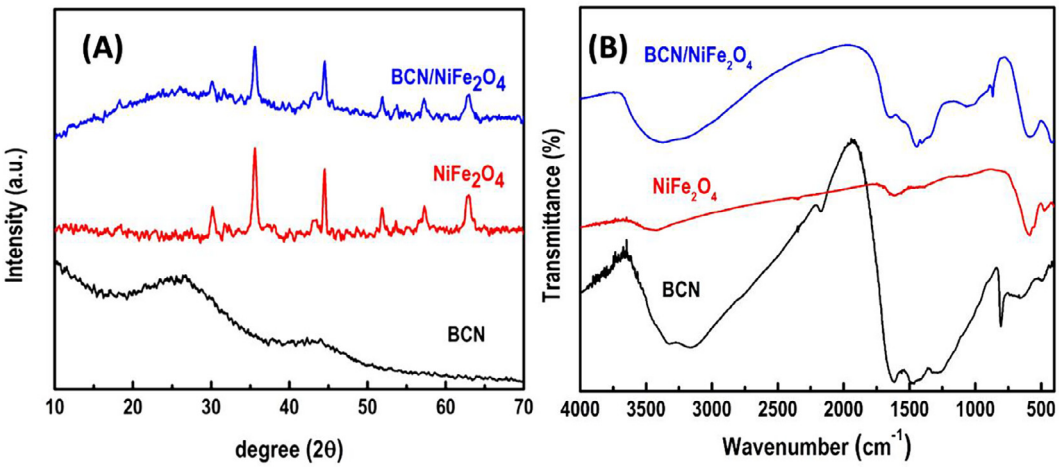

Fig. 1. (A) XRD patterns of as-synthesized BCN, $NiFe_2O_4$ and BCN/$NiFe_2O_4$ nanocomposite. (B) FT-IR spectra of BCN, $NiFe_2O_4$ and BCN/$NiFe_2O_4$ nanocomposite.

properties of BCN with $NiFe_2O_4$ could enhance the photocatalytic activity of organic dyes than that of the pure BCN and $NiFe_2O_4$.

In this present work, we report the synthesis of BCN/$NiFe_2O_4$ nanocomposite for the first time. The as-prepared BCN/$NiFe_2O_4$ nanocomposite was used as a novel visible-light catalyst for the photodegradation of organic dye, and methylene blue (MB) was used as a model dye for the photocatalytic measurements. The photocatalytic activity of BCN, $NiFe_2O_4$ and BCN/$NiFe_2O_4$ towards the degradation of MB was studied and discussed in detail. The photocatalytic degradation mechanism of MB using the photocatalyst has also been discussed.

Experimental

Materials

Iron chloride ($FeCl_3$, 98%, Alfa Aesar, WH, USA), nickel chloride ($NiCl_2{\cdot}6H_2O$, Sigma Aldrich, MO, USA), boric acid (H_3BO_3, J.T. Baker, CV, PA), dicyandiamide ($C_2H_4N_4$, 99%, Alfa Aesar, UK), sodium hydroxide (NaOH, Nihon Shiyaku Industries Ltd., Taiwan) and double distilled water was used throughout the experiment. All chemicals used in this work were of analytical grade and were used as received.

Synthesis of BCN

BCN was prepared by thermal polycondensation reaction using dicyandiamide and boric acid [25]. Briefly, 1.68 g of dicyandiamide and 0.6 g of boric acid were evenly grounded using an agate mortar. Further, this mixture was placed into a crucible with a lid and heated in a muffle furnace at 550 °C for 3 h with a heating rate of 5 °C min^{-1}. The final powder was collected, washed with ethanol followed by water and dried in an oven for 5 h at 80 °C.

Preparation of BCN/$NiFe_2O_4$ nanocomposite

The following procedure was used for the preparation of BCN/$NiFe_2O_4$ nanocomposite. First, the dispersion of BCN (1 g) in 100 mL water was prepared using ultra-sonication method (30 min). About 0.46 g of $NiCl_2$ and 1.62 g of $FeCl_3{\cdot}9H_2O$ was added into the above dispersion with continuous stirring. The pH of the solution was maintained at pH ~13 using 3 M NaOH. Then, the emulsion was stirred for 1 h at 80 °C using magnetic stirrer and dried at 90 °C. The obtained powder was calcined for 3 h at 450 °C with a heating rate of 5 °C min^{-1}. The obtained sample was labeled as BCN/$NiFe_2O_4$ nanocomposite. The similar procedure was used for the preparation of the $NiFe_2O_4$ and was prepared without BCN.

Characterization

The structural patterns and crystallite size of the synthesized materials were analyzed by the X-ray diffractometer (XRD) PANanalytical X'Pert PRO instrument with CuKα radiation (λ = 1.5418 Å). The surface morphology and elemental analysis of as-synthesized nanocomposite materials were analyzed using a JEOL-JEM2100F transmission electron microscopy (TEM) and JEOL JSM-7100F field-emission scanning electron microscope (FESEM). Fourier-transform infrared (FT-IR) spectra were obtained by Perkin Elmer FT-IR spectrometer. The FT-IR sample pellets were prepared using KBr substrate with synthesized different materials. UV–visible diffuse reflectance spectra (UV-DRS) was analyzed using Cary 5000 UV–Vis-NIR spectrophotometer with an integrating sphere attachment. A spectralon blank was used as the reference. The X-ray photoelectron spectroscopy (XPS) was analyzed by JEOL JPS-9030. Photoluminescence (PL) spectroscopy was measured using Dongwoo-Ramboss 500i, Gyeonggi-Do, Korea.

Photodegradation experiments

For the degradation experiments, the MB was used as a model textile pollutant to evaluate the catalytic performance of as-synthesized materials. The Mercury-Xenon lamp (350 W, 0.33 mW cm^{-2}, Prosper Technology, Taiwan) light was used as a visible light source. For the experiment, 100 mL of MB (5 ppm) dye was mixed with 100 mg of BCN/$NiFe_2O_4$ nanocomposite. Before the light introduction, the above mixture was stirred for 30 min to obtain dye-catalyst adsorption equilibrium. At a preset time (5 min), about 4 mL of the dispersion was drawn and filtered for the UV measurements.

Results and discussion

Characterization of the as-synthesized materials

The structural and phase information of all the samples were characterized by XRD. Fig. 1A shows the two distinct diffraction peaks for typical BCN at 26.9° and 43.8° which can be indexed as (0 0 2) and (1 0 0) planes (JCPDS card No. 34-0421) [26]. The significant broad peak at (0 0 2) attributes to the higher inter-planar distance like boron nitride and graphite. The plane (1 0 0) is due to the in-plane reflections of BCN [27,28]. The diffraction peak pattern of $NiFe_2O_4$ detected at 30.15°, 35.65°, 44.49°, 51.95°, 57.24° and 62.96° which are designated by their corresponding indexes 220, 311, 400, 422, 511 and 440 respectively (JCPDS 74-2081) [24]. The peaks at 26.74°, 35.65°, 44.49°, 51.95°, 57.24°, 62.96° can be ascribed to the (0 0 2, 2 2 0, 3 1 1, 4 0 0, 4 2 2, 5 1 1 and 4 4 0) of BCN/$NiFe_2O_4$ nanocomposite. The results

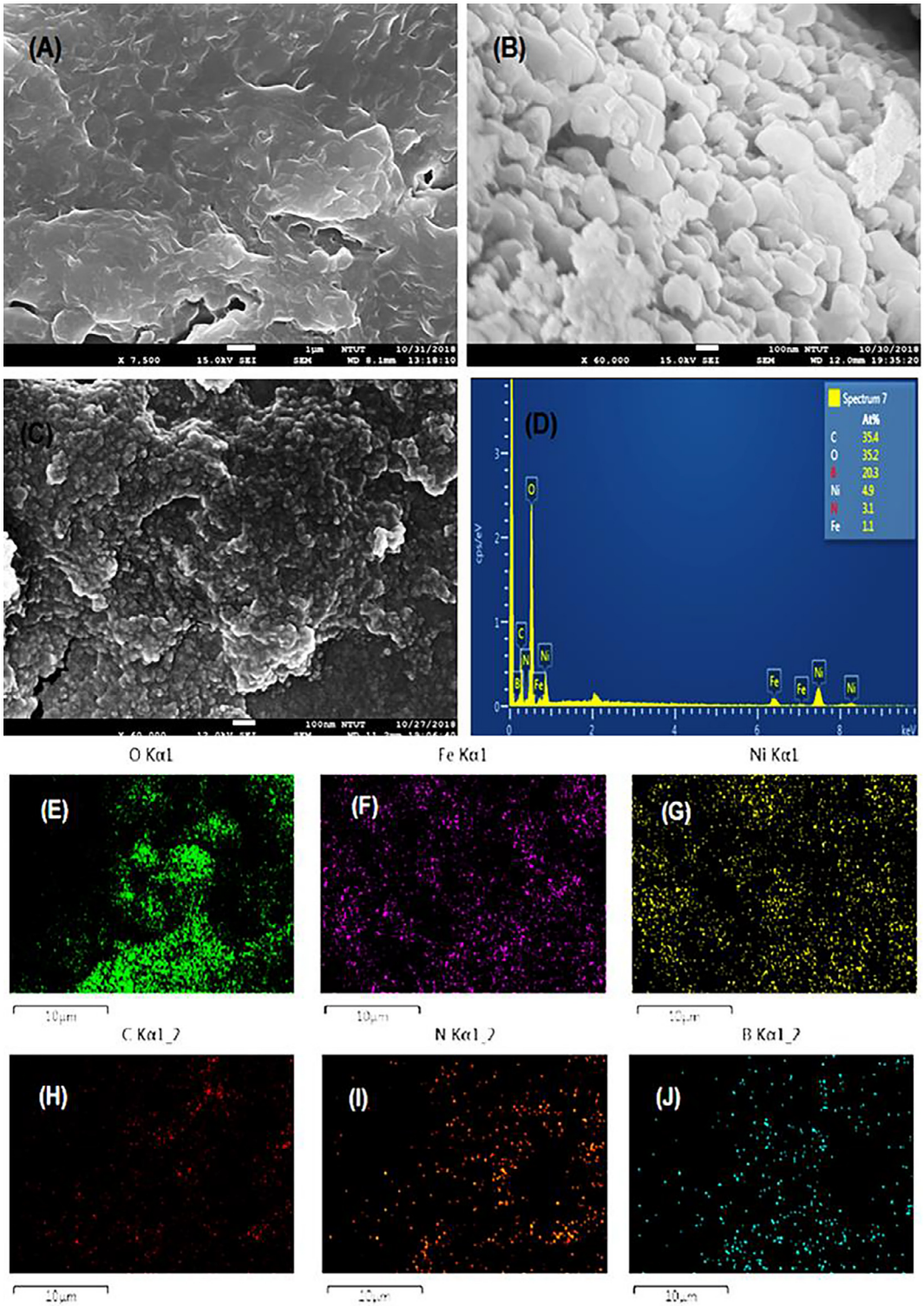

Fig. 2. FESEM images of BCN (A), $NiFe_2O_4$ (B), BCN/$NiFe_2O_4$ nanocomposite (C) and elemental analysis (D) and elemental mapping of O, Fe, Ni, C, N, and B (E–J) on BCN/$NiFe_2O_4$ nanocomposite.

confirmed the successful formation of BCN/$NiFe_2O_4$ nanocomposite.

The FT-IR spectra of BCN, $NiFe_2O_4$ and BCN/$NiFe_2O_4$ nanocomposites are shown in Fig. 1B. The $NiFe_2O_4$ and BCN/$NiFe_2O_4$ nanocomposite shows a broad vibration band at 3100–3500 cm^{-1} and is due to the stretching vibrations of N–H or O–H group. The peaks in BCN from 1200 to 1700 cm^{-1} can be attributed from the vibrational stretching band of C—N and C═N, and the peak around 806 cm^{-1} shows the band of triazine units [29]. The peaks of in-plane B—N and B—C are observed at 1462 and 1273 cm^{-1} respectively [30,31]. In $NiFe_2O_4$, the stretching vibrations of Fe—O bonds in tetrahedral positions and metal—O bonds in octahedral positions shows the sharp peak at 592 cm^{-1} and a weak peak at 466 cm^{-1} respectively [32]. For BCN/$NiFe_2O_4$ nanocomposite, the bands at 1652, 1450 and 579 cm^{-1} assigned to BCN, B—N vibration and Fe—O bonds respectively. The result confirmed that the structure of BCN and $NiFe_2O_4$ remains unchanged in the nanocomposite.

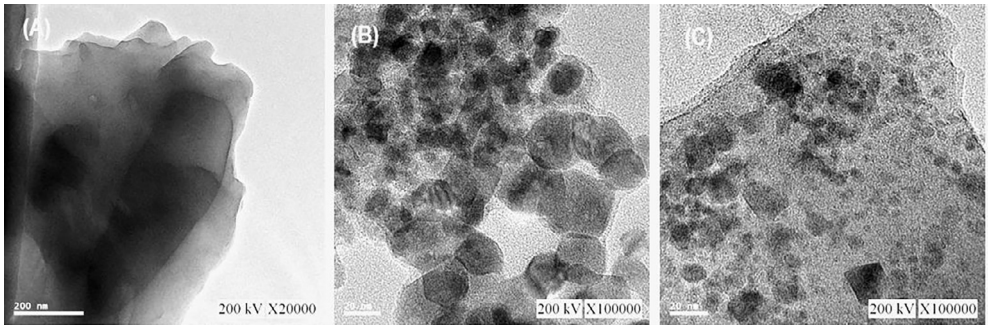

Fig. 3. TEM images of BCN (A), $NiFe_2O_4$ (B) and BCN/$NiFe_2O_4$ nanocomposite (C).

The surface morphology of the synthesized materials was analyzed by the FESEM, and the corresponding FESEM images are shown in Fig. 2. In Fig. 2A, a rough sheet-like structure was observed for BCN. Fig. 2B shows the aggregated particles of $NiFe_2O_4$ with the average diameter around 100 nm. This variable size of the particles is due to the synthesis process including milling in an agate mortar [33]. The Fig. 2C represents the BCN/$NiFe_2O_4$ nanocomposite with aggregated $NiFe_2O_4$ nanoparticles embedded on the sheet-like BCN. The size of the $NiFe_2O_4$ nanoparticles was reduced after incorporated with BCN than primary $NiFe_2O_4$ particles. The elemental analysis (Fig. 2D) and elemental mapping (Fig. 2(E–J)) results of the BCN/$NiFe_2O_4$ nanocomposite confirmed the presence of C, O, B, Ni, N, and Fe.

TEM was also performed to examine the structural morphology of as-prepared BCN, $NiFe_2O_4$ and BCN/$NiFe_2O_4$ nanocomposite. Fig. 3 shows the TEM images of BCN (A), $NiFe_2O_4$ (B) and BCN/$NiFe_2O_4$ nanocomposite (C). Fig. 3A shows the sheet-like structure of BCN and the agglomerated $NiFe_2O_4$ nanoparticles are visible in Fig. 3B. Fig. 3C confirmed that $NiFe_2O_4$ nanoparticles embedded on the surface of BCN. The obtained TEM images of BCN, $NiFe_2O_4$ and BCN/$NiFe_2O_4$ nanocomposite has found to similar to the morphology of FESEM.

The UV-DRS of the as-prepared composite material were measured in the wavelength ranges between 200 and 800 nm. Fig. 4A shows the UV-DRS of BCN, $NiFe_2O_4$ and BCN/$NiFe_2O_4$ nanocomposite. The BCN and $NiFe_2O_4$ show the band edge wavelengths in the visible light region of 200–800 nm. It can be seen that the band edge of the BCN/$NiFe_2O_4$ nanocomposite increases compared with BCN and $NiFe_2O_4$ which indicates the effective absorption of visible light by the BCN/$NiFe_2O_4$ nanocomposite than others. Fig. 4B shows the indirect bandgap of BCN/$NiFe_2O_4$ nanocomposite about 2.05 eV, and it was lower than that of BCN (2.65 eV) and $NiFe_2O_4$ (2.38 eV).

The surface elemental composition and the electronic state of the BCN/$NiFe_2O_4$ nanocomposite were characterized by XPS analysis and is shown in Fig. 5. The binding energies of B 1s, C 1s, N 1s, Ni 2p, Fe 2p and O 1s of the nanocomposite are shown in Fig. 5(A–F). The characteristic peak at 191.2 eV reveals the binding energy of B 1s and confirms the presence of B—N [34]. A broad peak of C1s includes C—C, C—O, C—N and C—B components appeared at binding energies of 284.9 eV, 288.4 eV, 285.6 eV, and 283.8 eV respectively [35]. The N 1s spectrum also includes the binding energies to pyridinic nitrogen at 398.6 eV, C—N—H group at 399.5 eV and graphitic nitrogen at 400.7 eV [36]. The binding energy of Ni $2p_{3/2}$ appears at 856.9 eV, and Ni $2p_{1/2}$ appears at 875.1 eV [37]. For the binding energy of Fe 2p appeared at 711.1 eV and attributed to Fe $2p_{3/2}$. The peak at 724.4 eV indicates the presence of Fe $2p_{1/2}$ [38]. The characteristic peak at 532.5 eV shows the O 1s in the $NiFe_2O_4$ composite at which is assigned for the O^{2-} and spinel metal oxides [38].

Photoluminescence spectroscopy

The PL spectra of BCN/$NiFe_2O_4$, $NiFe_2O_4$, and BCN, are shown in Fig. 6. A broad peak at 415 nm is observed for the BCN which exhibits the higher recombination rate of electron-hole pairs. Fig. 6 inset shows the reduced PL intensities of $NiFe_2O_4$ and BCN/$NiFe_2O_4$ which infers a significant reduction in the recombination rate when compared to BCN. There is a decrease in the emission peak intensity of BCN/$NiFe_2O_4$ which also indicates the effective e^-/h^+ charge separation and improved transfer efficiency from the valence band to the conduction band. Further, $NiFe_2O_4$ nanoparticles incorporated with BCN behaves as an electron acceptor and thus increases the photocatalytic activity.

Photo-catalytic degradation of MB

Fig. 7A shows the photo-catalytic degradation of MB by the as-prepared nanocomposite in the presence of visible light irradiation at a different time. It can be seen that the decrease in intensity at 664 nm with the increasing the visible light irradiation time. The result

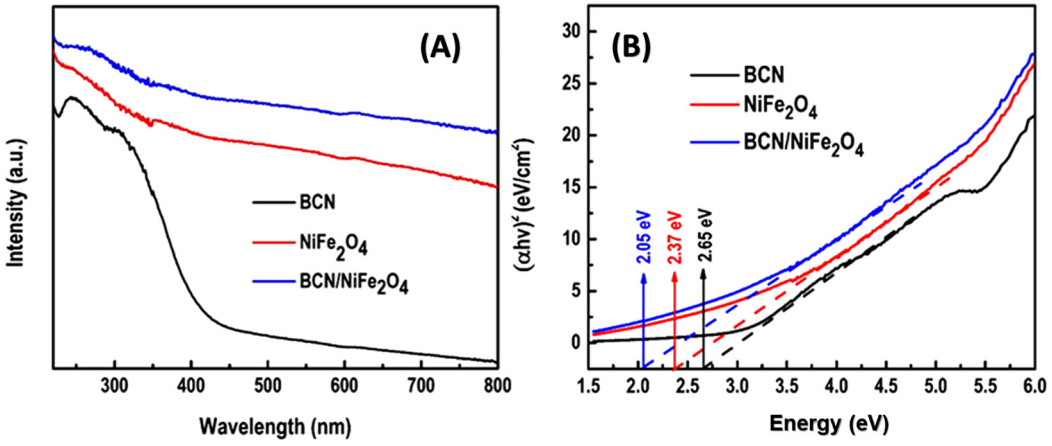

Fig. 4. UV-DRS of BCN, $NiFe_2O_4$ and BCN/$NiFe_2O_4$ nanocomposite (A), the indirect band gap of as-prepared BCN, $NiFe_2O_4$ and BCN/$NiFe_2O_4$ nanocomposite (B).

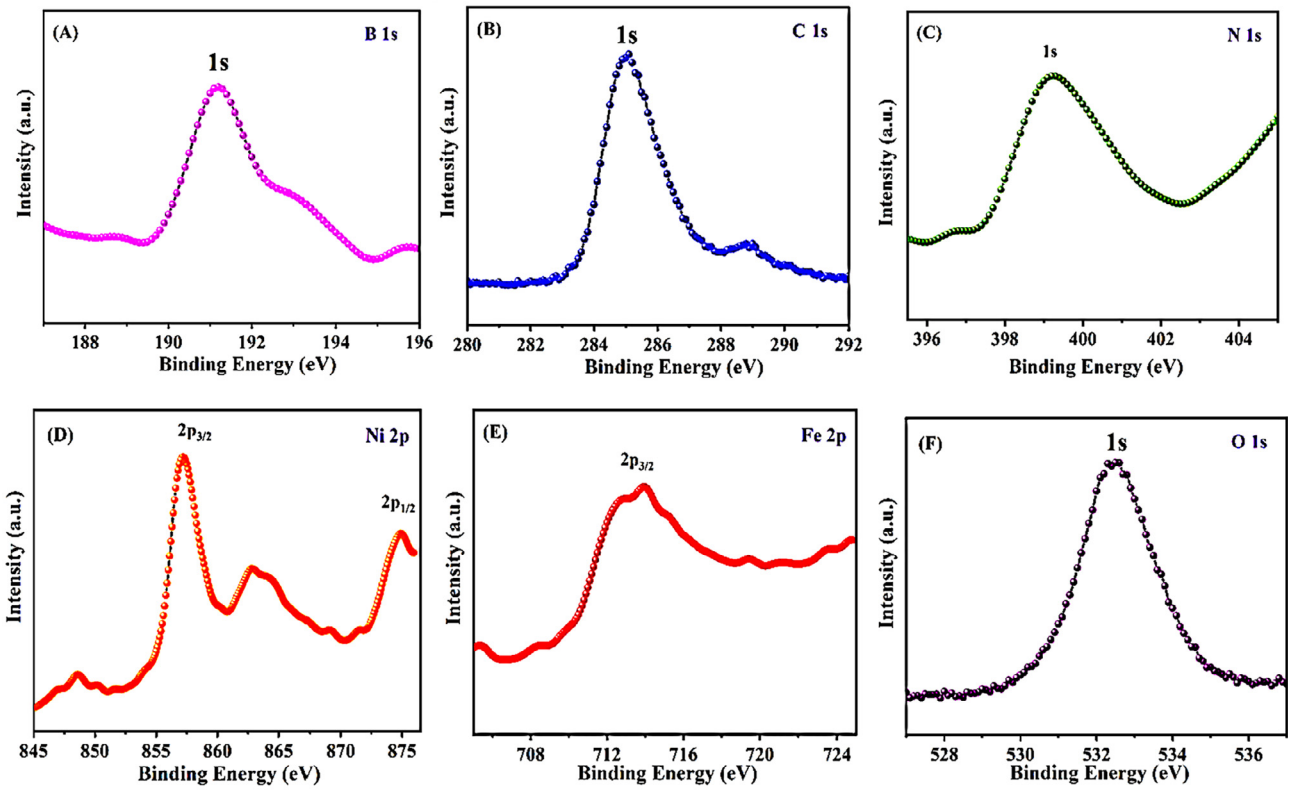

Fig. 5. High-resolution XPS spectra (B 1s, C 1s, N 1s, Ni 2p, Fe 2p, and O 1s) of as-synthesized BCN/$NiFe_2O_4$ nanocomposite.

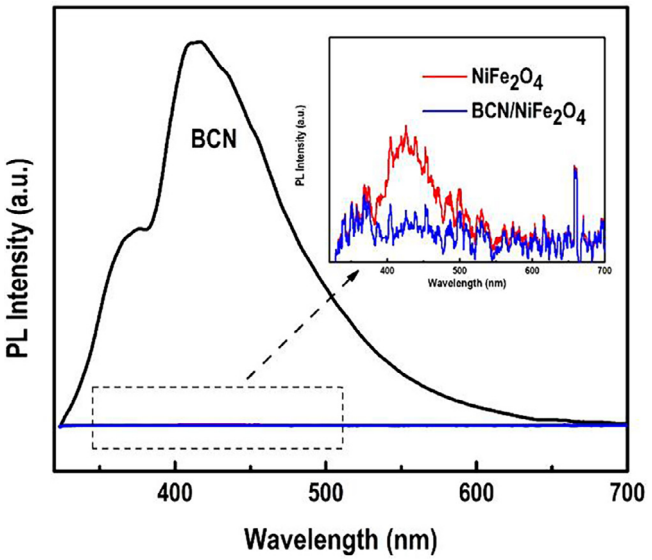

Fig. 6. PL spectra of BCN and $NiFe_2O_4$, BCN/$NiFe_2O_4$ nanocomposite (inset).

indicates the effective photodegradation of MB by the BCN/$NiFe_2O_4$ nanocomposite. A plot of time vs. the percentage of dye remaining in the solution is shown in Fig. 7B. The obtained results revealed that the degradation efficiencies of 25.6, 69 and 98% were obtained using $NiFe_2O_4$, BCN and BCN/$NiFe_2O_4$ nanocomposites at 80 min.

Photodegradation mechanism of MB

The synergistic effect between BCN and $NiFe_2O_4$ results in the enhancement in the photocatalytic activity and higher adsorption of MB on the catalyst surface. As discussed earlier that the as-synthesized nanocomposite has lower bandgap (2.05 eV) than that of BCN (2.65 eV) and $NiFe_2O_4$ (2.38 eV). The lower bandgap of the BCN/$NiFe_2O_4$ nanocomposite will help to achieve the enhanced photocatalytic activity towards the degradation of MB in the visible light region. Also, the recombination rate of BCN was reduced upon composite with $NiFe_2O_4$, and resulting in the higher electron-hole separation and a considerable population of e−/h+ pairs. The migration of electrons from the CB of BCN to the CB of $NiFe_2O_4$ causes a high negative (e^-) rich environment which also makes slightly positive VB of $NiFe_2O_4$. The holes on the VB of $NiFe_2O_4$ migrate to VB of BCN simultaneously. This process of redistribution of electrons-holes delays the recombination rate of the photoinduced carriers. The increased recombination rate of electrons and holes could reduce the catalytic activity due to the lack of producing $OH^{\cdot}$ and $O_2^{\cdot -}$. When the reaction medium introduced into the visible light irradiation, the valence band (VB) electrons were excited to the conduction band (CB), this photogenerated e− and h+ involved in the production of $OH^{\cdot}$ and $O_2^{\cdot -}$ radicals. The as-formed $OH^{\cdot}$ and $O_2^{\cdot -}$ radicals can oxidize the MB into the degradation products such as CO_2 and H_2O. The mechanism of the photodegradation of dye can be expressed by the following equations (Eqs. (1)–(4)).

$$BCN/NiFe_2O_4 + h\nu \rightarrow VB(h^+) + CB(e^-) \quad (1)$$

$$VB(h^+) + H_2O \rightarrow OH^{\cdot} + H^+ \quad (2)$$

$$CB(e^-) + O_2 \rightarrow \cdot O_2^- \quad (3)$$

$$OH^{\cdot} + \cdot O_2^- + \text{dye} \rightarrow \text{degradation products} \quad (4)$$

The kinetics and rate constant of the photocatalytic degradation reaction using $NiFe_2O_4$, BCN and BCN/$NiFe_2O_4$ are shown in Fig. 8A. A plot of ln(C/Co) vs. time follows the pseudo-first order kinetics. The rate constant (k′) value of BCN/$NiFe_2O_4$ nanocomposite ($k' = 4.4 \times 10^{-2}\,min^{-1}$) was obtained from the intercept of the linear line which was 12.7 times greater than $NiFe_2O_4$ ($k' = 3.5 \times 10^{-3}\,min^{-1}$) and 3.2 times greater than that of BCN ($k' = 1.4 \times 10^{-2}\,min^{-1}$). The correlation coefficient (R^2) values of BCN, $NiFe_2O_4$ and BCN/$NiFe_2O_4$ nanocomposite materials are found to

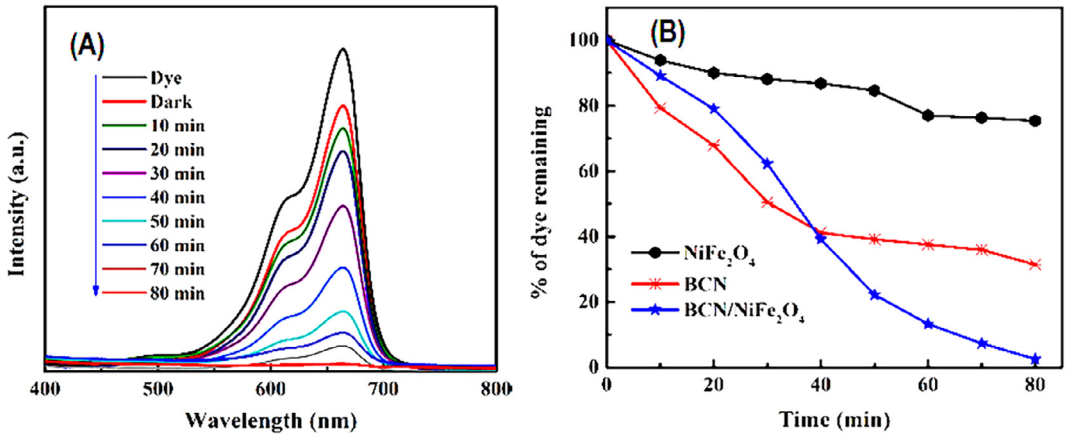

Fig. 7. Photocatalytic degradation of MB in the presence of BCN/$NiFe_2O_4$ nanocomposite (A). A plot of time vs. % of dye remaining in the solution (B).

be 0.9608, 0.9595 and 0.9796 respectively.

Reusability

The economic feasibility and practical usability of a photocatalyst material are analyzed with the reusability studies. Hence, the reusability studies of the BCN/$NiFe_2O_4$ nanocomposite are shown in Fig. 8B. After the degradation, the catalyst nanocomposite was collected by centrifugation. Then, it was washed with deionized water and ethanol to remove the adsorbed MB molecules and dried in an oven for 3 h. The collected nanocomposite was used subsequently to measure the photocatalytic efficiency. From the obtained results, the percentage degradation of MB was calculated to be 97.68%, 96.23% and 95.99% for three successive cycles. The result indicates the excellent cyclic stability of the BCN/$NiFe_2O_4$ nanocomposite.

To understand the role of the active species generated during the photocatalytic reaction, ethylenediaminetetraacetic acid (EDTA), $K_2S_2O_8$ (PP), acrylamide (AA) and tertiary butyl alcohol (T-BuOH) were used as the scavenger materials to trap holes (h^+), electrons (e^-), superoxide radicals ($\cdot O^{2-}$) and hydroxyl radicals ($\cdot OH$) respectively. The degradation process without scavengers shows 98% of MB degradation after 80 min. After the addition of EDTA, PP, AA, and T-BuOH scavengers into the system, the degradation percentage of MB was 81.2, 96.87, 44.0 and 85.1% respectively (Fig. 9). The results indicate that the contribution of active species in the photodegradation of MB as in the order of $\cdot O^{2-} > \cdot OH > h^+ > e^-$. Therefore, the degradation of MB significantly reduced because of the addition of AA to capture the $\cdot O^{2-}$. On the other hand, the degradation percentage of MB slightly decreased when PP, T-BuOH, and EDTA were added to the system.

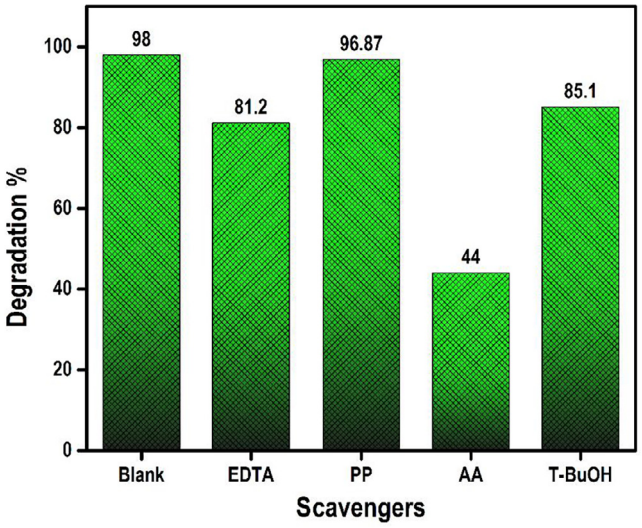

Fig. 9. Degradation % of MB using BCN/$NiFe_2O_4$ nanocomposite in the presence of different scavenging species (scavengers).

Conclusion

In conclusion, a novel BCN/$NiFe_2O_4$ photocatalyst was prepared by simple thermal condensation and sol-gel methods for the first time. The synthesized materials were confirmed by different physicochemical techniques. The as-synthesized nanocomposite material was used for

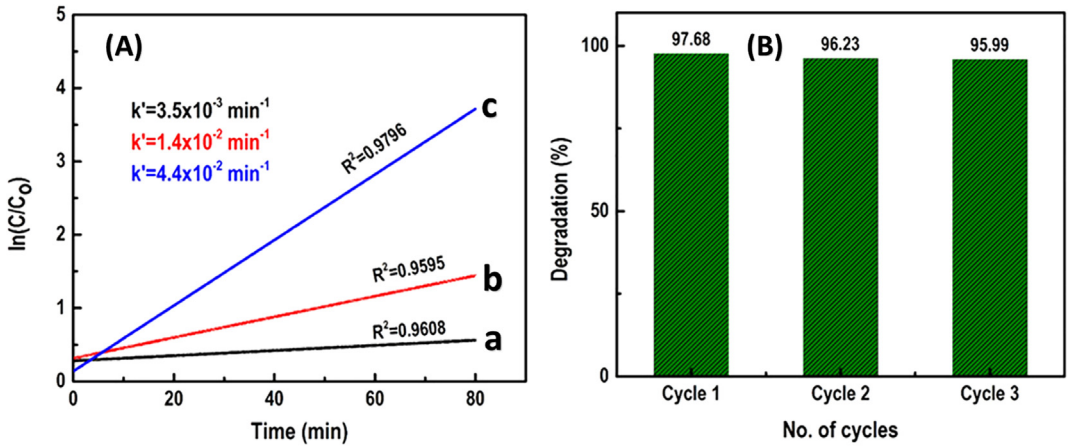

Fig. 8. (A) Pseudo-first order kinetics of photodegradation using $NiFe_2O_4$ (a), BCN (b), BCN/$NiFe_2O_4$ (c), and reusability of BCN/$NiFe_2O_4$ nanocomposite (B).

the effective degradation of MB. The obtained results revealed that BCN/$NiFe_2O_4$ nanocomposite had better catalytic activity towards MB than that of pristine $NiFe_2O_4$ and BCN. The degradation of the MB was confirmed by intensity variations of its UV absorption peaks, and the obtained results confirmed the pseudo-first-order kinetics mechanism. As a future perspective, the synthesized BCN/$NiFe_2O_4$ nanocomposite can be used as a low-cost photocatalyst material for the applications of environmental decontamination of organic dyes.

Conflicts of interest

The authors confirm that there are no conflicts to declare.

Acknowledgments

The authors would like to thank the Precision Analysis and Materials Research Centre, National Taipei University of Technology, Taipei, Taiwan for the financial support to this research.

References

[1] Houas, Lachheb H, Ksibi M, Elaloui E, Guillard C, Herrmann J-M. Photocatalytic degradation pathway of methylene blue in water. Appl. Catal. B 2001;31:145–57.
[2] Bukallah SB, Rauf M, AlAli S. Removal of methylene blue from aqueous solution by adsorption on sand. Dyes Pigm 2007;74:85–7.
[3] Akpan UG, Hameed BH. Parameters affecting the photocatalytic degradation of dyes using TiO_2-based photocatalysts: a review. J Hazard Mater 2009;170:520–9.
[4] Cripps, Bumpus JA, Aust SD. Biodegradation of azo and heterocyclic dyes by Phanerochaete chrysosporium. Appl Environ Microbiol 1990;56:1114–8.
[5] Balu S, Uma K, Pan G-T, Yang T, Ramaraj S. Degradation of methylene blue dye in the presence of visible light using SiO_2@ α-Fe_2O_3 nanocomposites deposited on SnS_2 flowers. Materials 2018;11:1030.
[6] Uma K, Balu S, Pan G-T, Yang T. Assembly of ZnO nanoparticles on SiO_2@α-Fe_2O_3 nanocomposites for an efficient Photo-Fenton reaction. Inorganics 2018;6:90.
[7] Namasivayam, Kavitha D. Removal of Congo Red from water by adsorption onto activated carbon prepared from coir pith, an agricultural solid waste. Dyes Pigm 2002;54:47–58.
[8] Métivier-Pignon H, Faur-Brasquet C, Le Cloirec P. Adsorption of dyes onto activated carbon cloths: approach of adsorption mechanisms and coupling of ACC with ultrafiltration to treat coloured wastewaters. Sep Purif Technol 2003;31:3–11.
[9] Han F, Kambala VSR, Srinivasan M, Rajarathnam D, Naidu R. Tailored titanium dioxide photocatalysts for the degradation of organic dyes in wastewater treatment: a review. Appl Catal A 2009;359:25–40.
[10] Wen J, Xie J, Chen X, Li X. A review on g-C_3N_4-based photocatalysts. Appl Surf Sci 2017;391:72–123.
[11] Zhang Y, Liu J, Wu G, Chen W. Porous graphitic carbon nitride synthesized via direct polymerization of urea for efficient sunlight-driven photocatalytic hydrogen production. Nanoscale 2012;4:5300–3.
[12] Dong G, Zhang Y, Pan Q, Qiu J. A fantastic graphitic carbon nitride (g-C_3N_4) material: electronic structure, photocatalytic and photoelectronic properties. J Photochem Photobiol C 2014;20:33–50.
[13] Mamba G, Mishra A. Graphitic carbon nitride (g-C_3N_4) nanocomposites: a new and exciting generation of visible light driven photocatalysts for environmental pollution remediation. Appl Catal B 2016;198:347–77.
[14] Zhang M, Bai X, Liu D, Wang J, Zhu Y. Enhanced catalytic activity of potassium-doped graphitic carbon nitride induced by lower valence position. Appl Catal B 2015;164:77–81.
[15] Xia P, Zhu B, Cheng B, Yu J, Xu J. 2D/2D g-C_3N_4/MnO_2 nanocomposite as a direct Z-scheme photocatalyst for enhanced photocatalytic activity. ACS Sustainable Chem Eng 2017;6:965–73.
[16] Deng Y, Tang L, Zeng G, Zhu Z, Yan M, Zhou Y, et al. Insight into highly efficient simultaneous photocatalytic removal of Cr(VI) and 2, 4-diclorophenolunder visible light irradiation by phosphorus doped porous ultrathin g-C_3N_4 nanosheets from aqueous media: performance and reaction mechanism. Appl Catal B 2017;203:343–54.
[17] Jiang L, Yuan X, Pan Y, Liang J, Zeng G, Wu Z, et al. Doping of graphitic carbon nitride for photocatalysis: a review. Appl Catal B 2017;217:388–406.
[18] Hou F, Li Y, Gao Y, Hu S, Wu B, Bao H, et al. Non-metal boron modified carbon nitride tube with enhanced visible light-driven photocatalytic performance. Mater Res Bull 2019;110:18–23.
[19] Hou Y, Wen Z, Cui S, Guo X, Chen J. Constructing 2D porous graphitic C_3N_4 nanosheets/nitrogen-doped graphene/layered MoS_2 ternary nanojunction with enhanced photoelectrochemical activity. Adv Mater 2013;25:6291–7.
[20] Liu Y, Song Y, You Y, Fu X, Wen J, Zheng X. $NiFe_2O_4$/g-C_3N_4 heterojunction composite with enhanced visible-light photocatalytic activity. J Saudi Chem Soc 2018;22:439–48.
[21] Zhao G, Liu L, Li J, Liu Q. Efficient removal of dye MB: through the combined action of adsorption and photodegradation from $NiFe_2O_4$/Ag_3PO_4. J Alloys Compd 2016;664:169–74.
[22] Gokon N, Murayama H, Nagasaki A, Kodama T. Thermochemical two-step water splitting cycles by monoclinic ZrO_2-supported $NiFe_2O_4$ and Fe_3O_4 powders and ceramic foam devices. Sol Energy 2009;83:527–37.
[23] Friebel MW, Louie M, Bajdich KE, Sanwald Y, Cai AM, Wise M-J, et al. Alonso-Mori, Identification of highly active Fe sites in (Ni, Fe) OOH for electrocatalytic water splitting. JACS 2015;137:1305–13.
[24] Peng T, Zhang X, Lv H, Zan L. Preparation of $NiFe_2O_4$ nanoparticles and its visible-light-driven photoactivity for hydrogen production. Catal Commun 2012;28:116–9.
[25] Zhang S, Gu P, Ma R, Luo C, Wen T, Zhao G, et al. Recent developments in fabrication and structure regulation of visible-light-driven g-C_3N_4-based photocatalysts towards water purification: a critical review. Catal Today 2018. https://doi.org/10.1016/j.cattod.2018.09.013.
[26] Pang J, Chao Y, Chang H, Li H, Xiong J, He M, et al. Tuning electronic properties of boron nitride nanoplate via doping carbon for enhanced adsorptive performance. J Colloid Interface Sci 2017;508:121–8.
[27] Liu X, Gao Y, Zhang M, Zhang X, Wang S, Feng B. Synthesis of fluorescent BCN hybrid nanosheets: a highly efficient fluorosensor for rapid, simple, sensitive Ag^+ detection. RSC Adv 2015;5:52452–8.
[28] Rivera-Tapia ED, Fajardo CA, Ávila-Vega ÁJ, Ávila CF, Sánchez-Arévalo FM, Chango-Villacís I, et al. Synthesis of boron carbon nitride oxide (bcno) from urea and boric acid, fullerenes, nanotubes. Carbon Nanostruct 2016;24:8–12.
[29] Lei W, Portehault D, Dimova R, Antonietti M. Boron carbon nitride nanostructures from salt melts: tunable water-soluble phosphors. JACS 2011;133:7121–7.
[30] Prakash A, Nehate SD, Sundaram KB. Boron carbon nitride based metal-insulator-metal UV detectors for harsh environment applications. Opt Lett 2016;41:4249–52.
[31] Kim DH, Byon E, Lee S, Kim J-K, Ruh H. Characterization of ternary boron carbon nitride films synthesized by RF magnetron sputtering. Thin Solid Films 2004;447:192–6.
[32] Zhu HY, Jiang R, Huang SH, Yao J, Fu FQ, Li JB. Novel magnetic $NiFe_2O_4$/multi-walled carbon nanotubes hybrids: facile synthesis, characterization, and application to the treatment of dyeing wastewater. Ceram Int 2015;41:11625–31.
[33] Moeinpour, Alimoradi A, Kazemi M. Efficient removal of Eriochrome black-T from aqueous solution using $NiFe_2O_4$ magnetic nanoparticles. J Environ Health Sci Eng 2014;12:112.
[34] Tian W, Shen Q, Li N, Zhou J. Efficient degradation of methylene blue over boron-doped g-C_3N_4/Zn0.8Cd0.2S photocatalysts under simulated solar irradiation. RSC Adv 2016;6:25568–76.
[35] Florent M, Bandosz TJ. Irreversible water mediated transformation of BCN from a 3D highly porous form to its nonporous hydrolyzed counterpart. J Mater Chem A 2018;6:3510–21.
[36] Zhang S, Gao L, Fan D, Lv X, Li Y, Yan Z. Synthesis of boron-doped g-C_3N_4 with enhanced electro-catalytic activity and stability. Chem Phys Lett 2017;672:26–30.
[37] Li X, Wang L, Zhang L, Zhuo S. A facile route to the synthesis of magnetically separable BiOBr/$NiFe_2O_4$ composites with enhanced photocatalytic performance. Appl Surf Sci 2017;419:586–94.
[38] Huang S, Xu Y, Xie M, Xu H, He M, Xia J, et al. Synthesis of magnetic $CoFe_2O_4$/g-C_3N_4 composite and its enhancement of photocatalytic ability under visible-light. Colloids Surf A Physicochem Eng Aspects 2015;478:71–80.